Data Specific Spatially Varying Regularization for Multimodal Fluorescence Molecular Tomography

Damon Hyde*, Eric L. Miller, Dana H. Brooks, and Vasilis Ntziachristos

Abstract—**Fluorescence molecular tomography (FMT) allows *in vivo* localization and quantification of fluorescence biodistributions in whole animals. The ill-posed nature of the tomographic reconstruction problem, however, limits the attainable resolution. Improvements in resolution and overall imaging performance can be achieved by forming image priors from geometric information obtained by a secondary anatomical or functional high-resolution imaging modality such as X-ray computed tomography or magnetic resonance imaging. A particular challenge in using image priors is to avoid the use of assumptions that may bias the solution and reduced the accuracy of the inverse problem. This is particularly relevant in FMT inversions where there is not an evident link between secondary geometric information and the underlying fluorescence biodistribution. We present here a new, two step approach to incorporating structural priors into the FMT inverse problem. By using the anatomic information to define a low dimensional inverse problem, we obtain a solution which we then use to determine the parameters defining a spatially varying regularization matrix for the full resolution problem. The regularization term is thus customized for each data set and is guided by the data rather than depending only on user defined *a priori* assumptions. Results are presented for both simulated and experimental data sets, and show significant improvements in image quality as compared to traditional regularization techniques.**

Index Terms—**Fluorescence, multimodality, tomography.**

I. INTRODUCTION

INTEREST in visualizing optical contrast in animals and humans, beyond the penetration limits of microscopy, has led to the development of imaging techniques such as fluorescence molecular tomography (FMT) [1]–[13]. Such methods can operate in absorption and fluorescence modes, enabling detection of biomarkers situated deep within target volumes [14]. While 2-D photographic imaging can be used for target detection, accurate localization and quantification of fluorescence distributions requires the use of tomographic techniques.

*D. Hyde is with the Computational Radiology Laboratory, Children's Hospital Boston, Harvard Medical School, Boston, MA 02115 USA (e-mail: damon. hyde@childrens.harvard.edu; dhyde@alum.wpi.edu).

E. L. Miller is with the Electrical and Computer Engineering Department, Tufts University, Medford, MA 02155 USA (e-mail: elmiller@ece.tufts.edu).

D. H. Brooks is with the Electrical and Computer Engineering Department, Northeastern University, Boston MA 02115 USA (e-mail: brooks@ece.neu.edu).

V. Ntziachristos is with the Institute for Biological and Medical Imaging, Technical University of Munich and Helmholtz Center Munich, D-85764 Munich, Germany (e-mail: v.ntziachristos@tum.de).

Modern tomographic systems operate in free-space geometries and avoid the use of matching fluids or optical fibers. These systems can additionally implement multi-angle projections and high spatial sampling of optical signals [15]. The less restrictive geometries and optimized data collection arising from these systems have yielded significant improvements in imaging capability as compared to older generation matching fluid-based or fixed geometry systems [15].

Despite these advances, optical tomography based on diffuse light offers an inherently low spatial resolution. Smoothness in the imaging kernel results in poor conditioning of the forward model, ultimately limiting resolution to approximately the millimeter scale and larger [1]. It has previously been reported that the use of structural information in the image formation process could help to compensate for this shortcoming [16]–[20]. High-resolution anatomical images, available from modalities such as X-ray computed tomography (XCT) and magnetic resonance imaging (MRI), can be segmented into structurally or functionally relevant regions. This information can then be used to improve both the forward and inverse aspects of the tomography problem. Techniques such as the finite element method (FEM) allow for solution of the diffusion problem on complex inhomogeneous tissue geometries, thereby improving the accuracy of the associated physical model. Additionally, the anatomical structure can be used to construct a prior model of the fluorescence image to be reconstructed. When applied to the inverse problem of recovering an image of the fluorescence distribution from a set of collected surface intensity measurements, this prior information can guide the reconstruction process to yield improved image accuracy.

In response, several methods currently have been proposed for constructing such prior models [16]–[20]. Most methods classify voxels in the high-resolution structural image according to tissue type. Registration between the modalities then allows the assignment of a tissue label to each voxel in the FMT reconstruction. This labeling divides the solution image into a number of segments, each comprising a group of voxels with a common tissue label. Regularization functionals are then established on each segment, based on assumptions of optical or functional characteristics for each tissue type. These functions can be based on known optical properties for the different tissue types, or can assume certain properties, such as smoothness of the solution or deviation from a mean in some or all of the tissue types [16], [17]. For example, employing a discretized Laplacian or Helmholtz operator for each region is useful when the image being reconstructed is expected to correlate highly with the anatomy. Another approach uses the labeling to define a separate Gaussian image prior on each region, and constructs a hierarchal Bayesian solution for imaging of endogeneous contrast

by using *a priori* estimates of the mean intensities on each region [18], [19].

The accuracy by which prior information is known strongly correlates with the performance of the hybrid method. When considering fluorescence solutions where little knowledge is generally known about the fluorescence biodistribution *a priori* the application of priors becomes more challenging. With the recent emergence of FMT-XCT [21] and FMT-MRI [22] approaches it becomes particularly important to develop methodologies that can benefit from the availability of high-resolution images without biasing the resulting solution. For this reason, we explore two aspects of the multimodality problem not directly considered in earlier reports. First, simply as a result of the imaging physics, multimodal imaging approaches generally use a high-resolution image to enhance a low-resolution image. In the case of FMT-XCT imaging, this means that each voxel in the low-resolution FMT reconstruction will cover several voxels in the high-resolution XCT image. While each XCT voxel is assigned a single anatomic type during the initial segmentation and tissue classification, FMT voxels near tissue boundaries will potentially span two or more tissue types. By associating each FMT voxel with only a single tissue type, errors in tissue labeling will result. (We note here that we use the term voxel to identify individual elements of the XCT or FMT images, while "segment" refers to a group of voxels that share a common tissue type labeling at either the XCT or FMT image scales.)

Second, existing methods typically use *a priori* assumptions which are applied in an identical manner to each data set. Smoothness constraints are applied uniformly to all segments, and prior estimates of signal intensity are likewise fixed for all data sets. However, each segment of each experimental volume may have unique intensity and smoothness levels, which should be taken into account if they are to be constrained by the prior model. Published hierarchal Bayesian approaches use fixed prior distributions for the hyperparameters, which are generally unavailable for fluorescence imaging. In both cases, these traits can often be defined using a small number of parameters, which, if estimated from the collected data, could provide customized prior models offering improved reconstruction results.

This type of customized regularization is potentially of great benefit for imaging fluorescent targets. While endogenous optical contrast is often well correlated with physical structure, the fluorescent probes imaged by FMT systems are specific to molecular activity levels which do not necessarily correlate perfectly with anatomy, and whose intensity levels are generally not known *a priori*. Accurate identification of active regions and subsequent selection of appropriate regularization levels would enable segments such as the background to be highly constrained, while permitting the remaining voxels in segments of higher activity to best account for the collected data.

To address these aspects, we introduce here a new space varying regularization technique for the incorporation of XCT or other high-resolution geometrical information into the solution of inverse diffusion problems. Our method first addresses the fundamental resolution differences by labeling each FMT solution voxel as a linear mixture of the tissue types identified in the high-resolution XCT image. At the interface between physical regions, the resulting prior model is then able to incorporate information from multiple regions, more accurately representing the underlying anatomy.

The labeling of segments is then used to create a low dimensional inverse problem that yields a single intensity value for each anatomic segment. We use these solution values as parameters to define a spatially varying regularization term for the full resolution FMT problem. The central idea of this paper is to use information present in the data in order to replace user-defined priors with data-driven priors. The underlying benefit is that the reduced dimensionality problem is not as ill-posed as the complete FMT inversion problem. It can thus yield more accurate information about mean values of the fluorescence biodistribution within each segment.

To showcase the performance of the method we studied two inversion implementations within the photon diffusion regime assuming a mouse brain geometry. Results are shown from simulated data and from *in vivo* measurements obtained for a recently reported experimental study [21]. We show that robust inversion can be obtained from a variety of fluorescence distributions and that in all cases the proposed method performs significantly better than standalone methods that do not utilize prior information.

This paper is structured as follows: Section II presents the forward and inverse models, as well as our method for the incorporation of *a priori* structural information. Section III contains details of the methods and materials used in our validation experiments. Results for both simulated and *in vivo* data sets are presented in Section IV, while Section V presents discussion, conclusions, and future work.

II. MODELING

For source-detector separations of more than a few millimeters, the propagation of light through tissue can be modeled by the diffusion approximation [23]. Using a spatially localized impulse function as the source term, Green's function solutions are computed either in analytical form for a number of specific geometries, or in the general case using numerical techniques such as the finite element method (FEM). The first order Born approximation then states that given these Green's functions, an equation for the received fluorescence can be written as [24]

$$U_{fl}(r_d, r_s) = Q_E^{\lambda_{fl}} \Theta_f^{fl} \int d^3 r \Theta_{\text{det}}(r_d) G_0^{\lambda_{fl}}(r_d, r)$$
$$\cdot \frac{\nu}{D^{\lambda_{fl}}} x(r) \Phi_o^{\lambda_{\text{exc}}}(r, r_s) \Theta_{\text{src}}(r_d). \quad (1)$$

Thus, the fluorescence detected at a point r_d as the result of a point source at r_s is modeled as the integral of diffused light from all fluorescent sources within the volume, given $\Phi_o^{\lambda_{\text{exc}}}$, the spatial distribution of excitation light. Here, $G_0^{\lambda_{fl}}(r_d, r)$ is the Green's function describing light propagation at the fluorescence wavelength. The parameters Θ_{det} and Θ_{src} are the source and detector coupling coefficients, ν and $D^{\lambda_{fl}}$ are the speed of light in tissue and the diffusion coefficient, $Q_E^{\lambda_{fl}}$ is the quantum efficiency of the camera at the fluorescence wavelength, and Θ_f^{fl} is fluorescence filter attenuation. The unknown spatial distribution of fluorochrome is represented here by $x(r)$.

Accurately determining the value of $\Phi_o^{\lambda_{\text{exc}}}$ requires solution of a second diffusion model, coupled to the first, describing light propagation at the excitation wavelength. For the imaging of fluorescent probes, the values obtained in this solution are often of little interest, and thus computation of $\Phi_o^{\lambda_{\text{exc}}}$ represents an additional, undesirable computational burden. An alternative approach, referred to as the normalized Born approximation, or simply, the Born ratio, has previously been introduced as a modeling method which bypasses the need to explicitly compute $\Phi_o^{\lambda_{\text{exc}}}$ [24]. By using corresponding measurements at the excitation wavelength to normalize the collected fluorescence measurements, the Born ratio has been shown to provide a significant degree of invariance to inhomogeneities in the imaging medium. Furthermore, it allows for the use of easily obtainable Green's functions in place of Φ in (1), greatly simplifying the image reconstruction formulation. Using a single Green's function to express the excitation wavelength measurements as:

$$U_{\text{exc}}(r_s, r_d) = Q_E^{\lambda_{\text{exc}}}\Theta_f^{\text{exc}}\Theta_{\text{det}}(r_d)G_0^{\lambda_{\text{exc}}}(r_d, r_s)\Theta_{\text{src}}(r_s) \quad (2)$$

the Born ratio can then be written as

$$\begin{aligned} U(r_s, r_d) &= \frac{U_{fl}(r_s, r_d)}{U_{\text{exc}}(r_s, r_d)} \\ &= \frac{Q_E^{\lambda_{fl}}}{Q_E^{\lambda_{\text{exc}}}}\frac{\Theta_f^{fl}}{\Theta_f^{\text{exc}}}\frac{\nu}{D^{\lambda_{fl}}} \\ &\quad \times \frac{\int d^3 r G_o^{\lambda_{fl}}(r_d, r)x(r)G_o^{\lambda_{\text{exc}}}(r, r_s)}{G_o^{\lambda_{\text{exc}}}(r_d, r_s)} \end{aligned} \quad (3)$$

where the excitation wavelength Green's function $G_0^{\lambda_{\text{exc}}}$ has replaced Φ in the equation for $U_{fl}(r_s, r_d)$. Source and detector coupling coefficients cancel out, leaving only fundamental system properties as free parameters, the values of which can be determined by calibration experiments.

To obtain a numerical inverse solution, the above integral equation can be discretized using a piecewise constant voxel basis. The resulting dependence of each measurement point upon individual voxels in the imaged volume is thus

$$\begin{aligned} W(r_s, r_d, r) &= \frac{Q_E^{\lambda_{fl}}}{Q_E^{\lambda_{\text{exc}}}}\frac{\Theta_f^{fl}}{\Theta_f^{\text{exc}}}\frac{\nu}{D^{\lambda_{fl}}} \\ &\quad \times \frac{G_o^{\lambda_{fl}}(r_d, r)x(r)G_o^{\lambda_{\text{exc}}}(r, r_s)\Delta V(r)}{G_o^{\lambda_{\text{exc}}}(r_d, r_s)} \end{aligned} \quad (4)$$

where $\Delta V(r)$ is the volume of the voxel centered at r. Accounting for data from all source-detector pairs, the forward model can be written as a linear system

$$u = Wx. \quad (5)$$

The matrix W, of size $N_{\text{data}} \times N_{\text{voxels}}$, is in general poorly conditioned and not square, making direct inversion impossible. Instead, an estimate of the fluorescence distribution x giving rise to the collected data u is obtained using the least squares formulation:

$$\hat{x} = \arg\min_x \|Q(Wx - u)\|_2^2 + \lambda^2\|Lx\|_2^2 \quad (6)$$
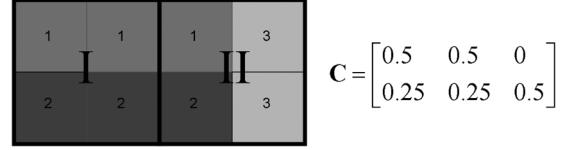

Fig. 1. Construction of partial volume labeling matrix. Here, voxel I lies 50% within region 1 and 50% within region 2, while voxel II lies 25% within region 1, 25% within region 2, and 50% within region 3. This is reflected in the rows of the matrix C, each of which is of unit one-norm.

where the regularization term L has been included to help stabilize the problem and the matrix Q represents the inverse square root of the noise covariance, as previously established for the Born ratio [25]. Additionally, this formulation implicitly assumes a zero mean model for the image x, an aspect we will address in more detail later. The parameter λ is used to control the degree of regularization, and its value is determined using methods such as the L-curve [26].

III. STRUCTURAL PRIORS

Given a CT or other structural image properly registered to the FMT coordinate system, individual voxels within the FMT image can be labeled with one or more tissue types. The segments arising from this labeling allow construction of a low dimensional problem that produces a single intensity value for each physical segment. These values can then be used to construct a dataset-adaptive spatially varying regularization term for use in the full resolution FMT problem, as explained below.

A. Low-Dimensional Parameterized Inverse

In order to employ structural information in the inverse problem, voxels in the FMT solution space must first be associated with the structural image. Modalities such as X-ray CT, however, have significantly better physical resolutions than FMT. Each FMT solution voxel will therefore occupy the same space as several voxels in the structural image. In the vicinity of tissue boundaries this difference in resolution means that each FMT voxel will potentially include more than one anatomic region. We propose to use a partial volume approach that models each FMT voxel as a mixture of multiple segments. This allows for the anatomical structure to be correctly related to the inverse problem.

Implementation of this voxel multiple-labeling, illustrated in Fig. 1, is done using a matrix, denoted as C, of size $N_{\text{voxels}} \times N_{\text{segments}}$. Here, N_{voxels} is the numbers of voxels in the full resolution FMT problem, while N_{segments} is the number of anatomic segments in the structural image. The individual elements C_{ij} are then defined as the fraction of voxel i which lies within segment j. Using this matrix, a parameterized version of the inverse problem in (6) can be written as

$$\hat{\mu}_x = \arg\min_{\mu_x}\|Q(WC\mu_x - u)\|_2^2 = \arg\min_{\mu_x}\left\|Q(\tilde{W}\mu_x - u)\right\|_2^2 \quad (7)$$

where $\tilde{W} = WC$, of size $N_{\text{data}} \times N_{\text{segments}}$ and $\hat{\mu}_x$ is a vector of length N_{segments}. This formulation is equivalent to obtaining an inverse solution using a piecewise constant basis defined by

the anatomical segmentation. Alternately, it can be seen as a method for estimating a mean fluorescence intensity for each tissue type or anatomical region. Conceptually, the idea is that by solving a reduced dimensional problem using the structurally defined basis, we can use the collected data to provide information about the fluorescence content of each region. We will then use this reconstruction to build a regularization matrix customized to each specific multimodal data set.

Because negative fluorescence concentrations are nonphysical, we must constrain the solution of (7) to be nonnegative. The low dimensionality of the parameterized problem allows us to use the modified residual norm steepest descent (MRNSD) approach without significantly increasing total computation time [27]. MRNSD requires a nonzero initialization, which we achieve using a normalized projection of the data onto the segments

$$\hat{\mu}_{xj}^{(0)} = \frac{1}{N_{\text{segments}}} \frac{u^T W_{*j}}{\|W_{*j}\|_2} \tag{8}$$

with $\tilde{W}_{*j}$ denoting the jth column of the matrix $\tilde{W}$. $\hat{\mu}_{xj}^{(i)}$ corresponds to the value associated with the jth region at iteration i.

B. Regularization Construction

Solution of (7) then yields a single value for each anatomic segment, which we will use in the construction of an appropriate spatially varying regularization term. If, as suggested earlier, these values are viewed as estimates of the mean for each segment, or alternately as an initial estimate of the image [28], then (6) could be modified to take the form

$$\hat{x} = \arg\min_x \|Q(Wx - u)\|_2^2 + \lambda^2 \|L(x - C\mu_x)\|_2^2 \tag{9}$$

which explicitly applies the μ_x values as spatially varying prior or initial estimates of mean intensity over the segments. This formulation also has a statistical interpretation as the maximum a posteriori (MAP) estimator of x, given the collected data u, noise covariance $(Q^T Q)^{-1}$, and the Gaussian image prior $x \sim N(C\mu_x, \lambda^{-2}(L^T L)^\dagger)$, with $\dagger$ representing the pseudoinverse.

Though optical contrast is often correlated with physical structure, the fluorescent probes that serve as the contrast agents for FMT imaging do not appear on a CT scan. Moreover, their ability to traverse anatomical boundaries means it is possible for probe to be located within only a small portion of a physical segment, be present within more than one segment, or even be contiguous across an anatomical border. Thus, the assumption of a uniform mean across the entire segment may not strictly hold for fluorescence imaging. As we will show in the results section, improved reconstructions can be obtained even when this assumption is not explicitly satisfied. However, owing to these possibilities, we also consider the original minimization equation

$$\hat{x} = \arg\min_x \|Q(Wx - u)\|_2^2 + \lambda^2 \|Lx\|_2^2 \tag{10}$$

which does not explicitly impose mean values upon the solutions in each region, and can be interpreted as a MAP solution given the prior model $x \sim N(0, \lambda^{-2}(L^T L)^\dagger)$.

In both cases, the matrix L is constructed as a diagonal matrix, with spatially varying diagonal elements derived from the low dimensional solution:

$$L = \text{diag}(C\alpha). \tag{11}$$

We define $\alpha = f(\mu_x)$ for some function $f()$, with $\mathbf{C}$ the same matrix used in (7) to build the parameterized problem. Thus a regularization level is defined for each anatomic segment. Individualized regularization for each FMT voxel is then generated as a mixture of those intensities using the matrix $\mathbf{C}$. The function $f(\mu_x)$ can thus be seen in the statistical interpretation as generating the inverse of the standard deviation for each individual region. We assume that the intensity for each region obtained with the parameterized solution is proportional to the intensities present at the full voxelized resolution. Regions with a low parameterized solution value should thus be treated as background regions, and more heavily regularized, while high parameterized solutions will lead to corresponding regions with lower levels of regularization. To achieve this, we want to select the function $f(\mu_x)$ such that an increase in mean value corresponds to a decrease in the corresponding regularization level.

A straightforward choice for $f(\mu_x)$ which achieves this goal corresponds to a model where the variance is proportional to the mean, as in the Gaussian approximation to a Poisson process, resulting in the relationship

$$\alpha_i = \frac{1}{\sqrt{\mu_{xi}}}. \tag{12}$$

This choice for α_i is unstable for small values of μ_{xi}, which are expected to appear frequently as a result of the nonnegativity constraint applied by the MRNSD algorithm. In place of the above equation, we use the modified version

$$\alpha_i = \sqrt{\frac{(1 + \beta)\max(\mu_{xj}|\forall j)}{\mu_{xi} + \beta\max(\mu_{xj}|\forall j)}} \tag{13}$$

which constrains α_i to be in the range $\alpha_i \in [1, \sqrt{1 + 1/\beta}]$. This alteration prevents regions from being infinitely regularized as μ_{xi} goes to zero, which would be equivalent to applying a hard prior and not reconstructing values within that region. Our approach avoids this and allows fluorescence intensities to be reconstructed at any location within the volume, but more heavily penalizes their appearance within background regions.

The choice of β will have an impact on the resulting solution by modifying the range of regularization parameters assigned to individual regions. For example, as β tends towards zero, the range of regularization parameters widens, resulting in a relative increase in the regularization applied to all regions, except the one with the greatest mean value. The lower the mean value of a particular region, the greater the increase in regularization. For regions with a mean value of zero, regularization will become infinite as β goes to zero, effectively removing those voxels from the reconstruction. Alternately, as β is increased, $\beta\max(\mu_{xj})$ becomes the dominant term in the denominator and all regions will be regularized in an identical manner. For the results presented below, the value $\beta = 0.066$ was used for all examples. This value was found through numerical experimentation to offer sufficient range of regularization values such that

imaging artifacts were suppressed without suppressing activity in regions with low mean values.

C. Summary of Approach

Given an appropriately segmented anatomical image, coregistered to the solution image, our approach can be summarized as follows.

1) Use the segmentation to assign partial volume labels to each of the solution voxels, and construct the matrix C.
2) Solve (7) using MRNSD to obtain a single parameter value for each region.
3) Use the solution to compute the values of the α_i's using (13).
4) Construct the regularization matrix L using (11), and proceed to solve either (9) or (10).

IV. EXPERIMENTAL METHODS

To evaluate our spatially varying regularization technique, we investigated a range of simulated and experimental data sets imaging amyloid-β plaques in the brains of transgenic mice exhibiting the symptoms of Alzheimer's disease. These plaques exist only within the brain, and are known to preferentially form within the cortical region. The experimental details and presentation of the *in vivo* data have recently been reported [21]. Here, we use this data to showcase the performance of the two inversion approaches presented herein, and to compare them to conventional inversions that do not utilize priors. We additionally provide corresponding simulations that allow further insight into the validity of the *in vivo* results. The data from the Alzheimer's model selected here yield a challenging tomographic problem, because the fluorescent targets are distributed throughout the volume, and not contained to a single small region.

A. In Vivo Imaging

In vivo experimental data was collected using a fluorescence molecular tomography system based on the non-contact multiangle collection of data in a transmission geometry [15]. As shown in Fig. 2(a), translation stages were used to appropriately position the source laser, while a rotation stage provided the ability to collected data from multiple projection angles. Data collection was done using an electrically cooled charged coupled device (CCD) camera (Roper Scientific, Trenton, NJ), positioned in a transillumination configuration. To provide surface localization information, silhouette images were collected at 360 projection angles. These images were used in conjunction with a previously described volume carving algorithm to localize the external surface of the animal [29].

The experimental group comprised APP23 transgenic mice exhibiting amyloid-β plaques characteristic of Alzheimer's disease, with C52Bl/6 mice providing controls. Two hours prior to imaging, each animal was given 100 mg/k of AO1987, an oxazine derivative probe which has previously been shown to exhibit specific binding with amyloid-β plaques [30]. Fluorochrome excitation was achieved using a 650 nm diode laser (BWTek, Newark DE). A total of 17 evenly spaced data collection angles were used, with an 0.6 cm × 0.6 cm grid of
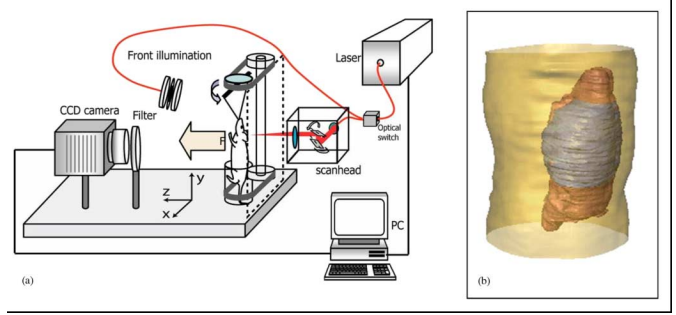

Fig. 2. (a) Noncontact FMT imaging system diagram. (b) Surface reconstructed with FMT system (yellow) overlaid with brain (red) and cortical (blue) segments obtained from CT structural image.

5 × 3 source locations used at each projection. For each angle, an 0.6 cm line of 10 detector points was used for each source location.

Excitation measurements were collected using a bandpass filter (three cavity interference, 652 ± 9.5 nm, Andover, Salem MA), while fluorescence measurements were collected with a combination of a bandpass filter (three-cavity interference 710 ± 10 nm, Andover, Salem, MA) and a longpass filter (Cutoff 695 nm; Omega Optical, Brattleboro, VT). To prevent CCD saturation, images at the excitation wavelength were collected with a 1.5OD filter placed between the animal and laser fiber. Fluorescence measurements were collected without this filter present to maximize received signal.

All internal anatomic information was provided by a single CT data set, collected from a C52bl/6 control mouse on an X-SPECT small animal imaging system (Gamma Medica, Northridge, CA). Given that the relative skull geometry is highly similar between animals, an affine transform was used to coregister the CT data set with the computed exterior surfaces using the eyes, teeth and base of skull as fiducial markers. Semi-automatic segmentation was achieved using the software package AMIRA (Visage Imaging, Carlsbad, CA). Because of the preferential formation of plaques in the cortex, the cortical region and remaining brain tissue were assigned as separate segments. This differentiation was used as prior knowledge in the inverse problem, while the forward model treated the entire brain as a single optically homogeneous region. Finite element method (FEM) solutions to the diffusion approximation were obtained using COMSOL (COMSOL, Inc, Burlington, MA) to construct the linear model for simulated data generation and all inversions.

B. Mouse Brain Simulation Studies

One *in vivo* imaging geometry, consisting of an eternal surface and coregistered brain and cortical segmentations, was selected for use in simulation studies. A series of imaging targets were computed on this geometry to evaluate algorithmic performance in a realistic structure. These targets were constructed to emulate scenarios expected to be seen *in vivo*, as well as more artificial targets to test algorithm performance. The first test case is a simple arrangement, with each voxel more than 50% within the cortex assigned an intensity as a sample of a single nonzero mean Gaussian process.

The second test case uses the same cortex voxels, but applies a spatially varying mean value to the Gaussian process. The maximum is at the centerline of the head, and decreases linearly as it moves away to the left and right. Test case three is the same as test case two, with the addition of low level fluorescence within the remaining brain tissue. Test case number four has two small fluorescing regions within the cortex, while cases five and six have a spatially varying intensity within a portion of the cortex that overlaps two subsegments (as described below), without and with the addition of background fluorescence elsewhere. Data for each case were generated using a linear normalized Born model, with 10% shot noise added.

C. Anatomic Subsegmentation

In initial experiments, large changes in the parameterized solution occurred with very small changes in the data or initialization, indicating poor conditioning of the reduced dimensional system. Further examination revealed that certain anatomical configurations result in a high degree of linear dependence among the columns of $\tilde{W}$ (the matrix in (7) of size $N_{\text{data}} \times N_{\text{segments}}$ resulting from the aggregation of voxels belonging to each segment). The columns of $\tilde{W}$ associated with the cortical and remaining brain tissue segments were highly correlated. This made it extremely difficult for the MRNSD algorithm to discriminate between segments, leaving the reconstructed parameters highly dependent upon initialization of the algorithm.

To correct this problem, we investigated the effects of subdividing the brain and cortex into smaller subsegments. For the work presented here, this was done in a purely geometrical manner, without taking the physical model or other attributes into account. We considered subdivision of both the central brain and cortical segments. The central brain was either left as a single segment, or divided into left and right hemispheres. To subdivide the cortex, the segment's centroid was located, and used as the reference point for dividing the cortex into $N \in \{1, 2, \ldots, 10\}$ subsegments, using an equal central angle subdivision scheme. This process is illustrated in Fig. 3.

For each configuration of subdivisions, the reduced dimensional matrix $\tilde{W}$ was generated for analysis. To analyze the matrix, the angle between each pair of columns was computed as [31]

$$\cos(\theta_{ij}) = \frac{\tilde{W}_{*i}^T \tilde{W}_{*j}}{||\tilde{W}_{*i}|| ||\tilde{W}_{*j}||}. \tag{14}$$

The average of these angles was taken across all pairs of columns, to generate a single average measure of the linear dependence present across columns of $\tilde{W}$. As can be seen in Fig. 3(b), this average angle rapidly increases with the number of cortical segments until it levels off at approximately $63°$ when seven segments are used. This suggests that some level of subdivision of the cortex should help stabilize the reconstructions, but that there is a diminishing return from each additional subsegment. Interestingly, introducing subdivision of the central brain [indicated by the triangles in Fig. 3(b), (c)] only reduces the average angle by approximately 4 degrees as compared to leaving it in undivided.
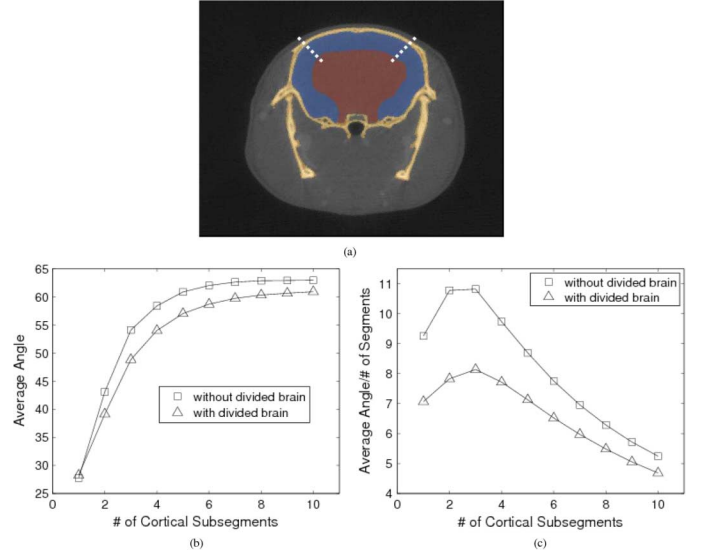

Fig. 3. Anatomic segmentation and subsegmentation. (a) The original segmentation separated the brain and brain cortex segments (red and blue segments, respectively), from the remaining soft tissue. Subsegmentation of the cortex divided it into three equal angle subsegments, as denoted by the white dashed lines. (b) Plot of number of cortical subsegments against resulting average angle between segments, with (triangle) and without (square) subdivision of the central brain segment. (c) Average angle divided by total number of subsegments plotted against number of cortical subsegments. Maximum is seen when cortex is divided into three subsegments.
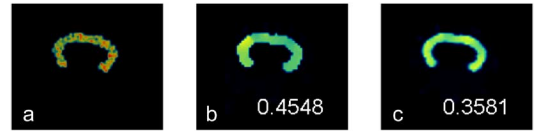

Fig. 4. Effects of partial volume labeling: (a) original image, (b) reconstruction without partial volume labeling, and (c) reconstruction employing partial volume labeling.

Our goal is to minimize the number of additional subsegments introduced, thus preserving as much of the initial segmentation as practical. As a metric to measure the increased complexity against the benefits of increased average angle, we divided the average angle by the total number of subsegments used. As shown in Fig. 3(c), this metric has a maximum when the cortex is divided into three subsegments, and the remainder of the brain remains whole. Thus, the subdivision scheme for all reconstructions presented below used a total of five segments for the low dimensional solution: three cortical subsegments, one segment for the remainder of the brain, and one segment for the background tissue.

V. RESULTS

A. Partial Volume Labeling Simulations

Fig. 4 shows results for a simulated data set with fluorescence present evenly throughout the cortical region. Fig. 4(b) shows reconstructions where each FMT voxel was assigned a single tissue type, while Fig. 4(c) is a reconstruction of the same dataset using partial volume labeling. The original image used to generate the data is shown in Fig. 4(a). Without the use of partial labeling, the structure of the segmentation is clearly visible,
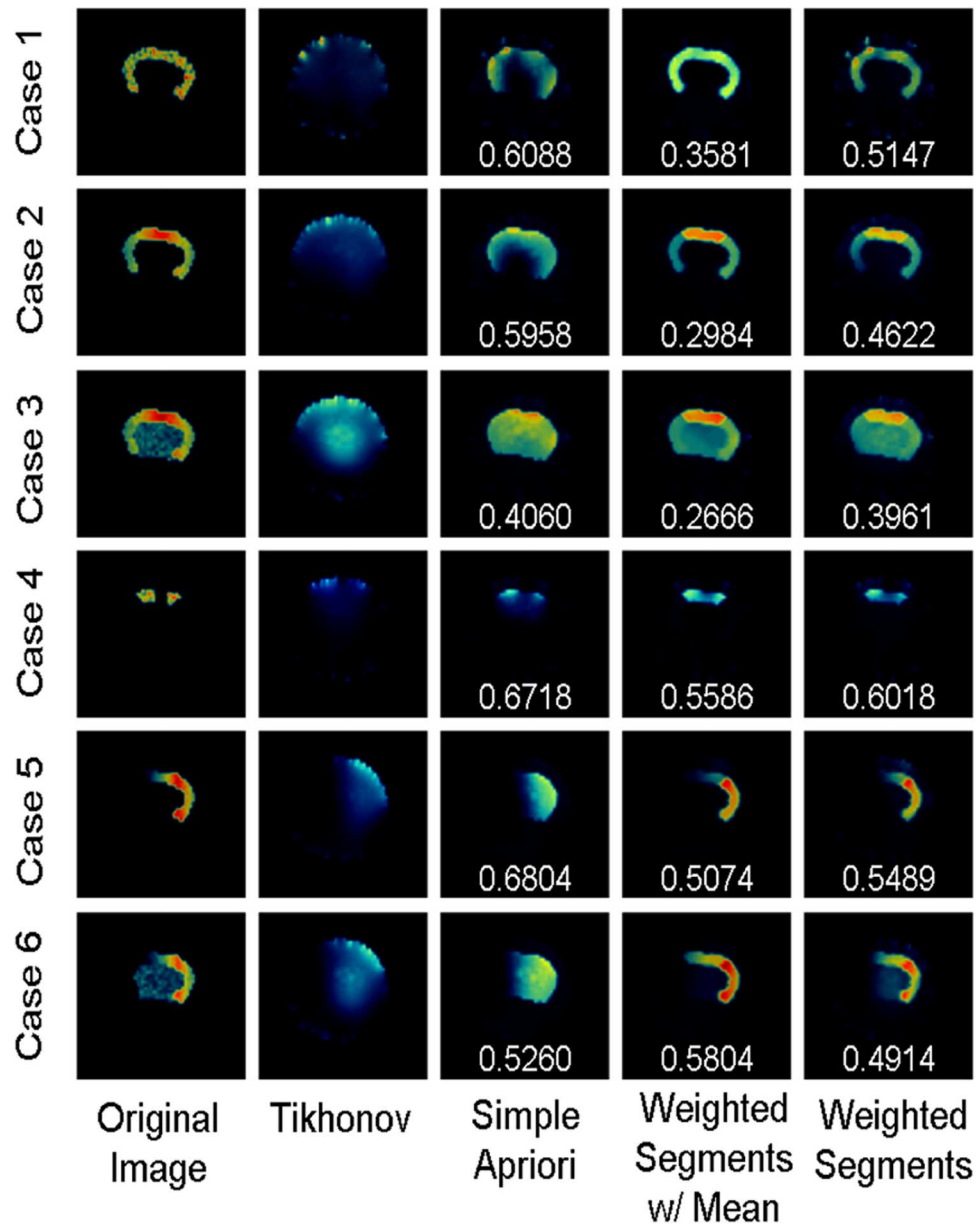
Fig. 5. Reconstructions for five simulated imaging cases. Ground truth is shown in the first column, while results using Tikhonov regularization with the identity matrix are in the second column. The simple *a priori* technique in the third column restricts the solution to either brain segment. The fourth and fifth columns show reconstructions using the techniques developed in Section III, with and without explicitly imposing a mean value in the image prior model, respectively. Overlaid numbers indicate relative 2-norm error with respect to ground truth.

with hard edges and right angle corners that are not present in the original image. By incorporating partial volume labeling, however, these artifacts can largely be eliminated, yielding a reconstruction with a much more natural appearance. Additionally, as indicated by the overlaid numerical values, the use of partial volume labeling reduces the relative 2-norm error present in the solutions.

B. Spatially Varying Regularization Simulations

Fig. 5 shows inversion results for each of the simulated datasets. The original images are seen in the first column, while the second column shows reconstructions using standard Tikhonov regularization with the identity matrix. In all cases, these reconstructions fail to recover either the location or

intensity of the fluorescence activity. Instead, they are heavily corrupted by surface artifacts, and the more deeply situated fluorescence is blurred throughout the volume. Clearly, the identity matrix is an inappropriate regularization choice for imaging of the distributed phenomenon of interest.

The reconstructions in column 3 are obtained by applying a simple *a priori* technique which regularizes voxels outside the brain segments in the CT segmentation four times as heavily as those within. This has the effect of largely constraining the reconstruction to the brain segment by heavily penalizing solutions with fluorescence within the surrounding soft tissue. There are two primary reasons this approach was chosen over one which simply restricts the solution to the brain region. First, for the *in vivo* datasets, there may be some low level of fluorescence
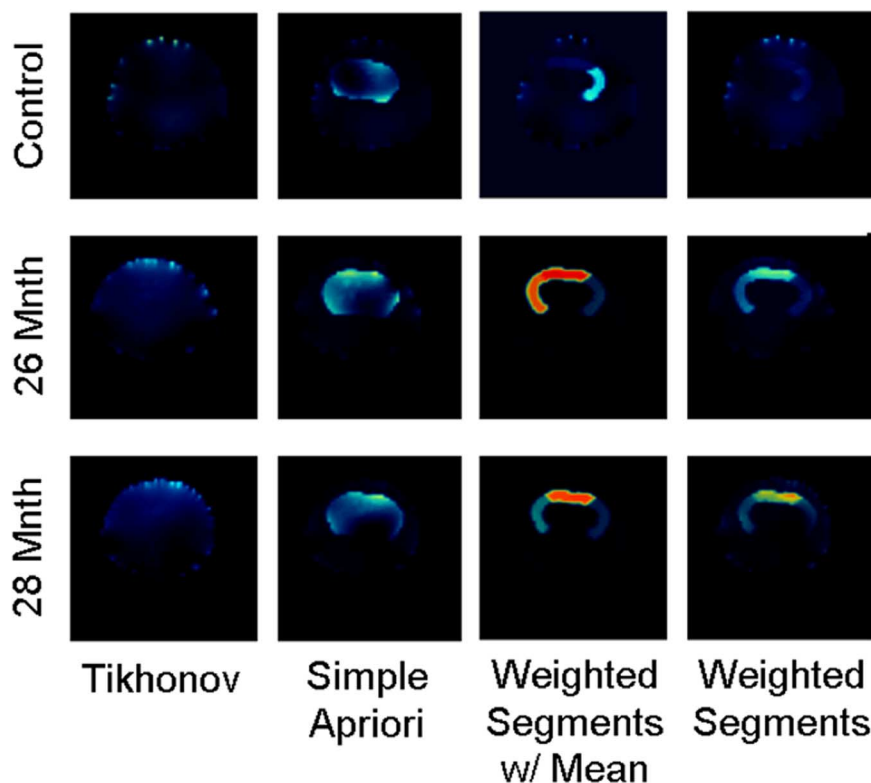
Fig. 6. Reconstructions for three *in vivo* mouse imaging studies. A control animal is shown in the first row, while APP23 transgenic animals exhibiting amyloid-β plaques in the cortical segment (ages 26 and 28 months) are shown in the second and third rows. The first column shows reconstructions using Tikhonov regularization with the identity matrix, while the second columns using a simple *a priori* technique which favors solutions in the brain region. The third and fourth columns show reconstructions using the techniques developed in Section III, with and without explicitly imposing a mean value in the image prior model, respectively.

present within the background. Second, using this ratio of regularization parameters allows a more direct comparison against the effects our proposed approach. Given our choice of $\beta =$, the maximum ratio of regularization parameters will be four to one. These reconstructions show a marked improvement over reconstructions using the identity matrix. The fluorescence is now inside the brain, but the different segments within the brain are not distinct, and the reconstructions still have a largely diffuse nature. For example, in test cases 5 and 6, the entire brain is resolved to have approximately the same fluorescence intensity, although the original images have higher intensity in the cortical segment.

Reconstructions using our method with both region dependant means and variances are shown in the fourth column. Here we see a much better differentiation of the cortical region, as compared to the reconstructions where the images is simply restricted to lying within the brain, and a closer resemblance to the original images. Relative two-norm error with respect to ground truth is also significantly reduced. However, these reconstructions yield highly uniform values on each of the regions, and fail to capture the shifting mean values seen in cases 5 and 6. These uniform values reflect the estimates of the mean value obtained in the first, low dimensional, inversion step. For datasets one, two, and three, where the voxels in each subsegment have similar intensities, the resulting reconstructions closely resemble ground truth. However, in test case six, applying the mean value actually performs worse with regards to 2-norm error than the simple *a priori* approach. Additionally,

the reconstructions clearly show artifacts from the segmentation and subsegmentation procedures, suggesting that a more complex, data-driven subsegmentation procedure may be useful for providing further improvements in the reconstructions.

Finally, the fifth column shows reconstruction results using our region dependent variance model, without the explicit use of mean values. As when we include explicit estimates of the mean values, the reconstructions obtained are improvements over both Tikhonov with the identity, and the simple *a priori* regularization technique. In case #1, additional artifacts can be seen as compared to the image in column 4, and this is reflected in a higher two-norm error. Reconstructions for cases 2–5 appear very similar to those obtained using the mean value, although the two-norm error is higher. In test case six, however, the reconstruction without the use of a mean value yields both the lowest two-norm error, as well as the greatest subjective similarity to the original image.

C. In Vivo Experiments

In vivo inversion results for three mice are shown in Fig. 6. The first row shows the results from a control animal, while the second and third rows show transgenic APP23 animals exhibiting the characteristics of Alzheimer's disease. Based on *ex vivo* examination, as reported in [21], we expect little fluorescence to be present within the control animal, and high concentrations of fluorescence throughout the cortical regions of the two afflicted animals.

As with the simulated results, reconstructions regularized with the identity matrix (first column) are heavily corrupted with surface artifacts and offer little in the way of subjective or quantitative information. The simple *a priori* method again yields image improvements. However undesirable features similar to those seen in the simulated data sets are still seen. The cortical fluorescence is again blurred into the central brain, and thus the reconstructions are not correctly representing the underlying fluorescence.

Using either of our approaches, with or without the use of a mean value, to incorporate the structural information, yields superior reconstructions suitable for further analysis. The control animal shows only very low fluorescence concentrations, possibly the result of unbound probe still present within the animal's bloodstream and nervous tissue. As expected, the two APP23 mice show high concentrations of fluorescence within the cortical region. The reconstruction do, however, place most of this reconstructed intensity within the dorsal subsegment of the cortex, possibly as a result of this region being closest to the surface, and thus having a higher sensitivity than more deeply situated regions.

VI. DISCUSSION AND CONCLUSIONS

We have presented here two variations on a method for the inclusion of *a priori* structural information in the reconstruction of images via data-informed multimodality space-varying regularization. This approach associates solution voxels with their underlying tissues types, and then regularizes voxels based on these associations rather than imposing a prior structure directly on the solution. We achieve this by using a multiple label map to define a low dimensional parameterized problem which yields information about the relative importance of each region to the overall reconstruction. These values are then used to construct a space-varying regularization term based on the tissue labeling of each voxel. Applied to simulated and *in vivo* localization of amyloid-β plaques in the brains of transgenic mice exhibiting the traits of Alzheimer's disease, our results indicate that both variations are highly effective at improving localization of fluorochrome distributions *in vivo*.

Simulation studies demonstrate that even with perfect model information, accurate reconstruction of spatially distributed fluorescent inclusions can be a difficult problem without prior knowledge of the underlying anatomical structure. The smoothness of the kernel and ill-posed nature of the problem bias it towards smooth solutions which do not reflect the underlying structure of the fluorescence distribution. Without the use of structural priors to compensate for this bias, reconstruction of distributed fluorescence becomes difficult, particularly for the challenging inverse problem formed by the target selected herein. By employing CT structural information in the reconstruction process, we are able to recover spatial and quantitative information with a much higher degree of accuracy than previously possible.

Our results also suggest that more investigation is necessary to determine the appropriate method for imposing mean values upon the solution. While explicitly applying a mean value provides improved two-norm performance in the majority of our simulations, the reconstructions obtained from experimental data appear overly constrained. We speculate that the relative performance of the two variations depends the uniformity of the fluorescence distribution within each region, as well as the presence or absence of low level background fluorescence. However, the exact nature of this performance and its relationship to the underlying fluorescence is currently unclear, and is a topic for future investigation.

One of the future efforts that will extend this work is the development of hybrid FMT-XCT systems capable of collecting all necessary data in parallel. The first major benefit would be having CT data specific to the mouse being imaged. While skulls can be matched to one another with reasonable accuracy using an affine transform, the use of more complex physical models would require the use of correspondingly more accurate anatomical information. While a CT collected in a separate system would suffice for imaging of the head, a significant amount of deformation is possible with other areas of the body. Thus the second benefit of a hybrid FMT-CT system would be that both data sets would view the animal in precisely the same orientation, and be accurately coregistered to one another. Given these advances, an obvious extension of this work would be its application to other imaging targets. Various tumor models have previously been studied [2], [32], and the addition of multimodal information would likely be of benefit, especially in the case of tumors located deep within the abdominal cavity.

Another potential avenue for future work would be the development of a more general approach for subsegmenting the original tissue labeling. In this paper, we used a geometric approach to subsegmentation that was specific to the geometry at hand, and applied it to stabilize the solution of the low dimensional problem. While some geometries may provide similar geometric subdivision schemes, other cases may require a more general approach. Such an approach could potentially involve tessellations of the volume, constrained by the geometry of the resulting subsegments. The results may also relate closely to those for the generation of multiresolution meshes for finite element modeling. Related to this would be a deeper analysis of the effects of subsegmentation upon the resulting reconstructions.

Finally, such an automated subsegmentation approach could be used to investigate the potential impact of using a larger number of subsegments in the reduced dimensional problem. Here, we simply sought to stabilize the reduced dimensional problem, while minimally perturbing the original segmentation. By subsegmenting into a larger number of regions, the mean values may better correlate with the true underlying fluorescence distribution. This might allow each individual pixel to be regularized in a more appropriate fashion, resulting in further improvements to reconstruction quality.

REFERENCES

[1] E. E. Graves, J. Ripoll, R. Weissleder, and V. Ntziachristos, "A submillimeter resolution fluorescence molecular imaging system for small animal imaging," *Med. Phys.*, vol. 30, no. 5, pp. 901–911, May 2003.

[2] V. Ntziachristos, E. A. Schellenberger, J. Ripoll, D. Yessayan, E. Graves, J. A. Bogdanov, L. Josephson, and R. Weissleder, "Visualization of antitumor treatment by means of fluorescence molecular tomography with an annexin v-cy5.5 conjugate," *Proc. Nat. Acad. Sci.*, vol. 101, no. 33, pp. 12294–12 299, Aug. 2004.

[3] A. Joshi, W. Bangerth, K. Hwang, J. Rasmussen, and E. M. Sevick-Muraca, "Plane-wave fluorescence tomography with adaptive finite elements," *Opt. Lett.*, vol. 31, no. 2, pp. 193–195, 2006.

[4] J. Lee and E. M. Sevick-Muraca, "Three-dimensional fluorescence enhanced optical tomography using referenced frequency-domain photon migration measurements at emission and excitation wavelengths," *J. Opt. Soc. Am. A*, vol. 19, no. 4, pp. 759–771, Apr. 2002.

[5] A. D. Klose and A. H. Hielscher, "Fluorescence tomography with simulated data based on the equation of radiative transfer," *Opt. Lett.*, vol. 28, no. 12, pp. 1091–1021, Jun. 2003.

[6] M. J. Eppstein, D. J. Hawrysz, A. Godavarty, and E. M. Sevick-Muraca, "Three-dimensional, Bayesian image reconstruction from sparse and noisy data sets: Neart-infrared fluorescence tomography," *Proc. Nat. Acad. Sci.*, vol. 99, no. 15, pp. 9619–9624, Jul. 2002.

[7] H. Jiang, "Frequency-domain fluorescent diffusion tomograph: A finite-element-based algorithm and simulations," *Appl. Opt.*, vol. 37, no. 22, pp. 5337–5343, Aug. 1998.

[8] M. A. O'Leary, D. A. Boas, X. D. Li, B. Chance, and A. Yodh, "Fluorescence lifetime imaging in turbid media," *Opt. Lett.*, vol. 21, no. 2, pp. 158–160, Jan. 1996.

[9] M. Eppstein, F. Fedele, J. Laible, C. Zhang, A. Godavary, and E. Sevick-Muraca, "A comparison of exact and approximate adjoint sensitivities in fluorescence tomography," *IEEE Trans. Med. Imag.*, vol. 22, no. 10, pp. 1215–1223, Oct. 2003.

[10] A. B. Milstein, S. Oh, K. J. Webb, C. A. Bouman, Q. Zhang, D. A. Boas, and R. Millane, "Fluorescence optical diffusion tomography," *Appl. Opt.*, vol. 42, no. 16, pp. 3081–3093, Jun. 2003.

[11] J. Chang, H. L. Graber, and R. L. Barbour, "Imaging of fluorescence in highly scattering media," *IEEE Trans. Biomed. Eng.*, vol. 44, no. 9, pp. 810–822, Sep. 1997.

[12] A. Kumar, S. Raymond, B. Bacskai, and D. Boas, "Comparison of frequency domain and time domain fluorescence lifetime tomography," *Opt. Lett.*, vol. 33, no. 5, pp. 470–472, 2008.

[13] A. B. Milstein, M. D. Kennedy, P. S. Low, C. A. Bouman, and K. J. Webb, "Detection and localization of a fluorescing mouse tumor in a turbid medium," *Appl. Opt.*, vol. 44, no. 12, pp. 2300–2310, Apr. 2005.

[14] V. Ntziachristos, J. Ripoll, L. V. Wang, and R. Weissleder, "Looking and listening to light: The evolution of whole-body photonic imaging," *Nature Biotech.*, vol. 23, no. 3, pp. 313–320, Mar. 2005.

[15] N. Deliolanis, T. Lasser, D. Hyde, A. Soubret, J. Ripoll, and V. Ntziachristos, "Free-space fluorescence molecular tomography utilizing 360 ° geometry projections," *Opt. Lett.*, vol. 32, no. 4, p. 382, Jan. 2007.

[16] P. Yalavarty, B. Pogue, H. Dehghani, and K. Paulsen, "Weight-matrix structured regularization provides optimal generalized least-squares estimate in diffuse optical tomography," *Med. Phys.*, vol. 34, no. 6, pp. 2085–2098, 2007.

[17] S. C. Davis, H. Dehghani, J. Wang, S. Jiang, B. W. Pogue, and K. D. Paulsen, "Image-guided diffuse optical fluorescence tomography implemented with laplacian-type regularization," *Opt. Exp.*, vol. 15, no. 7, pp. 4066–4082, Apr. 2007.

[18] X. Intes, C. Maloux, M. Guven, B. Yazici, and B. Chance, "Diffuse optical tomography with physiological and spatial a priori constraints," *Phys. Med. Biol.*, vol. 49, no. 12, pp. N155–N163, 2004.

[19] M. Guven, B. Yazici, X. Intes, and B. Chance, "Diffuse optical tomography with a priori anatomical information," *Phys. Med. Biol.*, vol. 50, no. 12, pp. 2837–2858, 2005.

[20] Y. Lin, H. Yan, O. Nalcioglu, and G. Gulsen, "Quantitative fluorescence tomography with functional and structural a priori information," *Appl. Opt.*, vol. 48, no. 7, pp. 1328–1336, 2009.

[21] D. Hyde, R. DeKleine, S. A. MacLaurin, E. Miller, D. H. Brooks, T. Krucker, and V. Ntziachristos, "Hybrid fmt-ct imaging of amyloid- β plaques in a murine alzheimer's disease model," *NeuroImage*, vol. 44, no. 4, pp. 1304–1311, Feb. 2009.

[22] V. Ntziachristos, A. G. Yodh, M. Schnall, and B. Chance, "Concurrent mri and diffuse optical tomography of breast after indocyanine green enhancement," *Proc. Nat. Acad. Sci.*, vol. 97, pp. 2767–2772, 2000.

[23] A. Kienle and M. S. Patterson, "Improved solutions of the steady-state and the time-resolved diffusion equations for reflectance from a semi-infinite turbid medium," *J. Opt. Soc. Am. A*, vol. 14, no. 1, pp. 246–254, 1997.

[24] V. Ntziachristos and R. Weissleder, "Experimental three-dimensional fluorescence reconstruction of diffuse media by use of the normalized born approximation," *Opt. Lett.*, vol. 26, no. 12, pp. 893–895, Jun. 2001.

[25] D. Hyde, E. Miller, D. H. Brooks, and V. Ntziachristos, "A statistical method for inverting the born ratio," *IEEE Trans. Med. Imag.*, vol. 26, no. 7, pp. 893–905, Jul. 2007.

[26] P. C. Hansen, "Analysis of discrete ill-posed problems by means of the l-curve," *SIAM Rev.*, vol. 34, no. 4, pp. 561–580, 1992.

[27] J. Nagy and Z. Strakos, "Enforcing nonnegativity in image reconstruction algorithms," in *Proc. SPIE Mathematical Modeling, Estimation, and Imaging*, D. C. Wilson, Ed.   Bellingham: WA, 2000, pp. 182–190.

[28] P. C. Hansen, Rank Deficient and Discrete Ill-Posed Problems ser. SIAM Monographs on Mathematical Modeling and Computation, 1998.

[29] T. Lasser, A. Soubret, J. Ripoll, and V. Ntziachristos, "Surface reconstruction for free-space 360 ° fluorescence molecular tomography and the effects of animal motion," *IEEE Trans. Med. Imag.*, vol. 27, no. 2, pp. 188–194, Feb. 2008.

[30] M. Hintersteiner, A. Enz, P. Frey, A.-L. Jaton, W. Kinzy, R. Kneuer, U. Neumann, M. Rudin, M. Staufenbiel, M. Stoeckli, K.-H. Wiederhold, and H.-U. Gremlish, "In vivo detection of amyloid- β deposits by near-infrared imaging using an oxazine-derivative probe," *Nature Biotechnol.*, vol. 23, no. 5, pp. 577–583, May 2005.

[31] G. H. Golub and C. F. V. Loan, *Matrix Computations*.   Baltimore, MD: John Hopkins Univ. Press, 1996.

[32] V. Ntziachristos, A. G. Yodh, M. D. Schnall, and B. Chance, "Mri-guided diffuse optical spectroscopy of malignant and benign breast lesions," *Neoplasia*, vol. 4, pp. 347–354, 2002.